ADVANCES IN ATMOSPHERIC SCIENCES, VOL. 31, SEPTEMBER 2014, 995–1008

Mesoscale Predictability of Moist Baroclinic Waves: Variable and Scale-dependent Error Growth

BEI Naifang*[1] and Fuqing ZHANG[2]

[1]*School of Human Settlements and Civil Engineering, Xi'an Jiaotong University, Xi'an* 710049
[2]*Department of Meteorology, the Pennsylvanian State University, University Park, Pennsylvania* 16802*, USA*

(Received 26 September 2013; revised 25 January 2014; accepted 13 February 2014)

ABSTRACT

This study seeks to quantify the predictability of different forecast variables at various scales through spectral analysis of the difference between perturbed and unperturbed cloud-permitting simulations of idealized moist baroclinic waves amplifying in a conditionally unstable atmosphere. The error growth of a forecast variable is found to be strongly associated with its reference-state (unperturbed) power spectrum and slope, which differ significantly from variable to variable. The shallower the reference state spectrum, the more spectral energy resides at smaller scales, and thus the less predictable the variable since the error grows faster at smaller scales before it saturates. In general, the variables with more small-scale components (such as vertical velocity) are less predictable, and vice versa (such as pressure). In higher-resolution simulations in which more rigorous small-scale instabilities become better resolved, the error grows faster at smaller scales and spreads to larger scales more quickly before the error saturates at those small scales during the first few hours of the forecast. Based on the reference power spectrum, an index on the degree of lack (or loss) of predictability (LPI) is further defined to quantify the predictive time scale of each forecast variable. Future studies are needed to investigate the scale- and variable-dependent predictability under different background reference flows, including real case studies through ensemble experiments.

Key words: predictability, baroclinic waves, error growth, mesoscale

Citation: Bei, N. F., and F. Q. Zhang, 2014: Mesoscale predictability of moist baroclinic waves: Variable and scale-dependent error growth. *Adv. Atmos. Sci.*, **31**(5), 995–1008, doi: 10.1007/s00376-014-3191-7.

1. Introduction

Since the pioneering work on predictability by Lorenz (1969) based on a low-order baroclinic model, a series of large-scale predictability studies have been performed with models that have varying degrees of complexity (e.g., Leith, 1965; Charney et al., 1966; Smagorinsky, 1969; Shukla, 1981; Lorenz, 1982). Based on some of these studies and the theory of homogeneous turbulence, Tennekes (1978) drew pessimistic conclusions concerning mesoscale predictability. On the other hand, Anthes et al. (1985) found little forecast divergence from simulations using different initial conditions in a limited-area mesoscale model, which implied potentially extended predictability, but their results were subsequently found to arise from the perfectly known lateral boundary conditions they employed (Errico and Baumhefner, 1987; Vukicevic and Errico, 1990), or from the poor resolution of the smaller scale instabilities (Zhang et al., 2002; Zhang and Snyder, 2003).

Analysis of observations indicates that the atmospheric kinetic energy spectrum follows a -3 power law at synoptic scales with a transition to a $-5/3$ power law within the mesoscale (Nastrom and Gage, 1985; Cho et al., 1999). Global and mesoscale model runs with high resolution have produced the spectra with a similar transition in slope (Koshyk and Hamilton, 2001; Skamarock, 2004; Zhang et al., 2006; Skamarock and Klemp, 2008; Hamilton et al., 2008). Spectra with a similar transition from -3 to $-5/3$ have also been found using high-resolution quasigeostrophic (QG) models (Tung and Orlando, 2003; Tulloch and Smith, 2006; 2009) and nonhydrostatic Boussinesq models (Bartello, 2010; Kitamura and Matsuda, 2010). An enstrophy downscale cascade from synoptic scales based on QG turbulence suggested by Charney (1971) has been widely accepted as the formation mechanism of the energy spectrum with -3 slope. The explanation of the mesoscale spectrum is more complicated and controversial. Past interpretations for the mesoscale spectrum can be divided into three categories: (1) an inverse cascade of energy from the small scales (Gage, 1979; Lilly, 1983; Vallis et al., 1997); (2) a forward cascade of nonlinearly interacting gravity waves (e.g., Dewan, 1979; VanZandt, 1982; Yuan and Hamilton, 1994); (3) a direct cascade of energy from the large scales (e.g., Koshyk and Hamilton, 2001; Lindborg and Cho, 2001; Tung and Orlando, 2003; Lindborg, 2006). Recently, Waite and Snyder (2013) found

* Corresponding author: BEI Naifang
Email: bei.naifang@mail.xjtu.edu.cn

that the inclusion of moisture has a significant effect on the mesoscale kinetic energy spectra of baroclinic waves, which is also found in global model simulations (Hamilton et al., 2008).

Faster error growth, especially at smaller scales in the presence of parameterized moist convection, was first found by Ehrendorfer et al. (1999). Zhang et al. (2002) and Zhang and Snyder (2003) further explained the possible influence of small-amplitude and small-scale initial errors on mesoscale predictability of the "surprise" snowstorm of 24–25 January 2000. Tan et al. (2004) generalized the above-mentioned results through examining the error growth in idealized baroclinic waves amplifying in a conditionally unstable atmosphere. They additionally demonstrated that there is little error growth in the short-term forecasts without the effects of moisture. The impacts of moist convection on the limit of mesoscale predictability demonstrated in these studies are consistent with what was foreseen in Lorenz (1969). In addition, Zhang et al. (2007) (hereafter, "Z07") proposed a multistage error growth conceptual model through exploring the mesoscale error growth dynamics in idealized moist baroclinic waves with the model grid spacing down to 3.3 km. Bei and Zhang (2007) studied the impacts of initial error scale and amplitude on the mesoscale predictability of heavy precipitation along the Mei-Yu front of China. They found that larger-scale, larger-amplitude initial uncertainties generally led to larger forecast divergence than did uncertainties of smaller scales and smaller amplitudes.

Hohenegger and Schär (2007) found much faster error growth rates and much shorter error-doubling time in cloud-resolving scales than those in synoptic scales. Rotunno and Snyder (2008) generalized the Lorenz model (Lorenz, 1969) and applied it to both the two-dimensional vorticity equation (2DV, with a -3 spectrum) and the surface quasigeostrophic equation (SQG, with a $-5/3$ spectrum) to produce examples of flows with unlimited and limited predictability. Morss et al. (2009) explored the link between spectral slopes and predictability behavior in a multilevel quasigeostrophic model with three different model resolutions and mentioned that the error growth rate varies with model resolution and model forecast time.

Although a number of studies on the spatial scale and model-resolution-dependent predictabilities have been conducted as we mentioned above, few studies have comprehensively investigated the predictability of different model forecast variables at different scales using different model resolutions. As an extension of Z07 and complementary to Morss et al. (2009), this study seeks to quantify the predictability of different forecast variables at different scales through explicit simulations of idealized moist baroclinic waves amplifying in a conditionally unstable atmosphere with different model resolutions. An index named LPI [an index on the degree of lack (or loss) of predictability] is defined to quantify the predictability of forecast variables, and its physical meaning is further examined through a two-dimensional (2D) spectral decomposition. The experimental design is introduced in section 2. The model effective resolution of the reference forecasts is discussed in section 3. The resolution and variable-dependent error growth and predictability are discussed in section 4. The scale and variable-dependent error growth and predictability are included in section 5. Further interpretations of LPI in physical space are given in section 6. The conclusions are summarized in section 7.

2. Experimental design

In this study, the fifth-generation Pennsylvania State University–National Center for Atmospheric Research Mesoscale Model (MM5) version 2 is used to simulate the idealized moist baroclinic waves with model grid spacings of 90, 30, 10 and 3.3 km (Fig. 1). The model employs Cartesian coordinates and a constant Coriolis parameter. As in Z07, we design the 90-km domain (D1) in a channel with a length of 18 000 km in the east–west direction and a width of 8010 km in the north–south direction. The 30-km domain (D2) is centered at (9720 km, 3960 km) inside D1, with a length of 8400 km in the east–west direction and a width of 4800 km in the north–south direction. The 10-km domain (D3) is a sub-domain with a length of 5800 km and width of 2800 km inside D2, while the 3.3-km domain (D4) is 1933 km long and 1333 km wide inside D3. The physical process parameterization schemes used in all domains include the Medium-Range Forecast (MRF) scheme (Hong and Pan, 1996) for PBL processes and the simple ice microphysics scheme (Dudhia, 1993). The cumulus parameterization of Grell (1993) is used only in domains D1 and D2. The initial conditions used in this study are the same as used in Z07 and Tan et al. (2004), in which a three-dimensional "balanced" perturbation (Rotunno and Bao, 1996, p. 1057) was added at the tropopause level of a two-dimensional baroclinically unstable jet with plentiful moisture. For the control experiment (CNTL), the model is integrated on D1 for 72 h using the above-mentioned initial conditions with fixed lateral boundary conditions (named as CNTL-D1 hereafter). We conduct three other experiments, including experiment CNTL-D2 with the nested domains of D1 and D2, experiment CNTL-D3 with the nested domains D2 and D3 initialized at

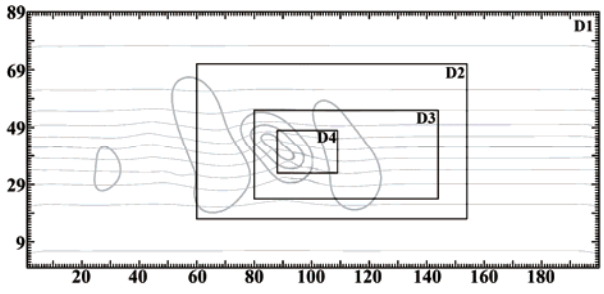

Fig. 1. The MM5 domains (D1, D2, D3 and D4). Also shown are the D1 simulated surface potential temperature (thin line, $\Delta = 6$ K) and sea level pressure (thick line, $\Delta = 8$ hPa) valid at 36 h of the coarsest grid (D1) forecast, which are used as the initial conditions for the nested domains. The distance between small tick marks is 90 km.

36 h of the CNTL-D1 forecast, and experiment CNTL-D4 with the three nested domains D2, D3, and D4. In CNTL-D4, two-way nesting is applied between domains D2 and D3 as well as between domains D3 and D4. The integration time of domains D2 and D3 are 36 hours, while that of domain D4 is 12 hours. In the perturbed runs, "grid-point (grid by grid data set)", random, Gaussian noises with zero mean and a standard deviation of 0.2 K are added to the temperature field at the initial time of domain D2 ($T_0 = 36$ h, referred to as CNTL-D2P). The initial perturbation used in domain D2 is interpolated onto domains D3 and D4 (referred to as CNTL-D3P, CNTL-D4P). For a more detailed description of the model setups and relevant idealized moist baroclinic wave simulations, refer to Z07.

Z07 performed an in-depth study on the error growth processes of the idealized moist baroclinic waves amplifying in a conditionally unstable atmosphere. They proposed a multistage error growth conceptual model, which included convective instability and saturation (0–6 h), transition and adjustment (3–18 h) and linear baroclinic growth (beyond 12 h). For these three stages, Fig. 2 shows the 500-hPa meridional wind (v) differences (between perturbed and unperturbed runs) at 3, 12, and 36 h along with the CNTL-D3 simulated 500-hPa height. It exemplifies rapid error growth in magnitude and spatial coverage between perturbed and unperturbed runs from 3 to 36 h.

Complementary to Z07, the current study seeks to quantify error growth of individual forecast variables. The two-dimensional spectral analysis obtained by conventional discrete Fourier transforms is used in this study. More specifically, for both reference and difference spectra calculations, the transforms are first performed in both directions (zonal and meridional) to obtain the 2D spectral coefficients with respect to the wavenumbers of both directions (k, l) for each variable at every model level (the decomposition domain is assumed to be doubly periodic after linear detrending). The 2D spectra are then converted to a 1D spectra through binning the sum of the power spectral coefficients that has the same global wavenumber $(\sqrt{k^2 + l^2})$. The spectra decomposition is conducted on every grid for each variable and then added together. The final power spectra analyzed here are averaged vertically over the model vertical levels. To quantify the error growth, we further define an index on the degree of LPI as the ratio of the difference or forecast error (between perturbed and unperturbed) spectral power to the reference (unperturbed) spectral power at a given scale or a range of scales. The time by which the LPI reaches 100% defines the predictable time scale—the threshold at which the forecast of this variable at a given scale no longer has predictive skill when the difference error energy (noise) is equal to or outweighs the basic-state energy (signal) to be predicted. This definition is consistent with Warner et al. (1983), who argued that "given a perfectly predictable large scale atmospheric structure, a measure of mesoscale predictability is the time required for a specified error in the mesoscale structure of one or more variables to cause the prediction of a specific quantity to be sufficiently in error so that it has essentially zero utility". For a pure sinusoidal wave without amplitude error, a 100% LPI amounts to a shift of the phase by 1/6 of the wavelength, or a correlation coefficient between the reference and perturbed waves of 50%. The level of correlation between the unperturbed and the perturbed fields is also often used for predictability measures (e.g., Islam et al., 1993).

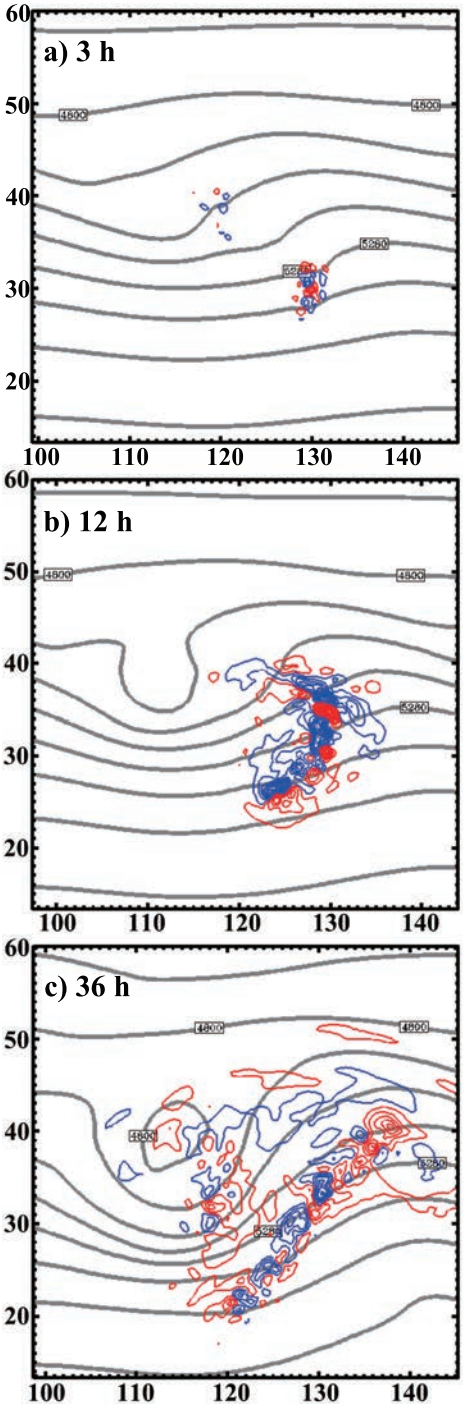

Fig. 2. The 500-hPa meridional wind difference (thin lines; $\Delta = 2$ m s^{-1}; positive, red; negative, blue) between 10-km perturbed and unperturbed runs valid at (a) 3 h, (b) 12 h, and (c) 36 h of the nested-domain simulations plotted on a subdomain of D2.

3. Base-state power spectra and model effective resolution of the reference forecasts

Using the spectral analysis method described in section 2, we first calculate the 2D power spectra of forecast variables of the control run with different model grid spacings (30, 10 and 3.3 km) in domain D4.

Figure 3 shows the reference spectra of the selected forecast variables at various model grid spacings and the corresponding spectral slope (green solid line, obtained through linear fitting) between 20 and 200 km wavelengths in the 3.3-km control run. With the finer model grid spacing, the spectra have a better-defined power-law regime for all variables. The reference spectra at different grid spacings match well at larger scales but differ at smaller scales for different variables. Skamarock (2004) first proposed the concept of the effective resolution of a model, in which they defined the effective resolution of a model as the wavelength where a model's spectrum begins to decay relative to the observed spectrum or relative to a spectrum from a higher-resolution simulation (which should resolve higher wavenumbers before numerical dissipation leads to decay). It is the smallest scale that the model can resolve with the present grid spacing. Figure 3 shows that the effective resolution of MM5 is around seven times the model grid spacing, consistent with the results using the Weather Research and Forecasting (WRF) model by Skamarock (2004). For example, in Fig. 3a, the minimum scale at which the spectral power of the 30-km (10-km) grid spacing forecast agrees with that from the 10-km (3.3-km) grid spacing run is around 210 km (70 km). Clearly, the spectrum of the reference state varies significantly with forecast variables and resolutions. Among the forecast variables, pressure has the steepest power-spectrum slope (-2.05), while vertical velocity has the shallowest (and a positive) slope (0.67). The spectral slope of zonal wind (u wind), temperature and pressure (-1.91, -1.96 and -2.05, respectively) are steeper than $-5/3$ [mesoscale behavior, e.g., Gage (1979), Nastrom and Gage (1985), Cho et al. (1999)]. The spectral slope of meridional wind (v), water vapor, hydrometeors (cloud) and precipitation (rain) (-1.73, -1.65, -1.50 and -1.68, respectively) are all close to $-5/3$. The reference spectrum of any given forecast variable reveals the strength of the spectral power of this variable at different scales (in terms of different wavenumber or wavelength), though it may not be an energy variable itself. The shallower the spectrum, the more energy at the smaller scales, and thus the less predictability for any given variable since the error grows faster at smaller scales before it saturates. Error saturation to the reference power usually signals a total loss of predictability at that scale. For example, cloud water has a shallow spectrum because it is directly related to smaller scale energy (directly associated with convective instability), thus it is less predictable.

In addition, the power spectra for the velocity variables (u, v and w) exhibit shallowing at scales of around 100 km (shown in Figs. 3a, b and e), which means that the slope is larger at larger scales but the slope becomes less steep from 100 km to smaller scales. The spectral slope here is a few times smaller than that at the transition scales of 400–500 km found in Hamilton et al. (2008) and Skamarock and Klemp (2008), but is consistent with a recent study of moist baroclinic waves (Waite and Snyder, 2013) and an observational study using aircraft data (Lindborg, 2007). For the peculiarity of the rain spectra (Fig. 3h), we speculate that such overlapping is due to the fact that the rain variable used in the present study is 1-h accumulated rainfall, which is a 2D time-integrated variable that is very different from the other 3D variables with instantaneous output.

4. Resolution and variable-dependent error growth and predictability

Section 3 showed that the power spectra of forecast variables of the control runs differ from each other and change with model resolution. In this section, we examine the predictability of forecast variables and their sensitivity to the model resolution.

As in Zhang et al. (2002), we use the difference total energy (DTE),

$$\mathrm{DTE} = \frac{1}{2}\sum (U'^2_{i,j,k} + V'^2_{i,j,k} + kT'^2_{i,j,k}) \ ,$$

to quantify the error growth between perturbed and unperturbed runs, where U', V' and T' are the difference wind components (zonal wind u and meridional wind v) and difference temperature between the perturbed and unperturbed (control or reference) simulations, $k = c_p T$ (control or reference) simulations, $k = c_p/T_\mathrm{r}$, in which c_p is the specific heat at a constant pressure of 1005.7 J K^{-1} kg^{-1}, T_r is the reference temperature of 270 K, and i, j and k run over x, y and z grid points.

The spectrum of DTE is then compared to that of the reference-state total energy [$\mathrm{TE} = \sum(U^2 + V^2 + kT^2)/2$] at different resolutions. Figure 4 shows the DTE and TE spectra at the model grid spacings of 30 and 10 km evaluated over the domain D3 (10-km domain) (Figs. 4a and b), and the DTE spectra at the model grid spacings of 10 and 3.3 km evaluated over D4 (3.3-km domain) (Figs. 4c and d). The gap between the green thin lines, which denotes difference spectra every 3 h (1 h), indicates the developing ratios of the error growth in 3 h (1 h), so the bigger the gap the faster the error growth. During the first several hours, according to the gap between the green thin lines, the error grows more rapidly at smaller scales and spreads to larger scales more quickly before the error saturates at those small scales in the simulation with the grid spacing of 10 km (see the green lines in Fig. 4b) in comparison with that of the 30-km simulation (see the green lines in Fig. 4a). As a result, comparing the reference total energy (solid lines—black for Fig. 4a and red for Fig. 4b), the DTE error saturates earlier at smaller scales than at larger scales in the higher-resolution simulations. The comparisons between 10 and 3.3 km (Figs. 4c and d) generally show the same results. As described in Zhang et al. (2007), this is consistent with the multiscale error growth of Lorenz (1969), in which the error first saturates at smaller scales, after which the error

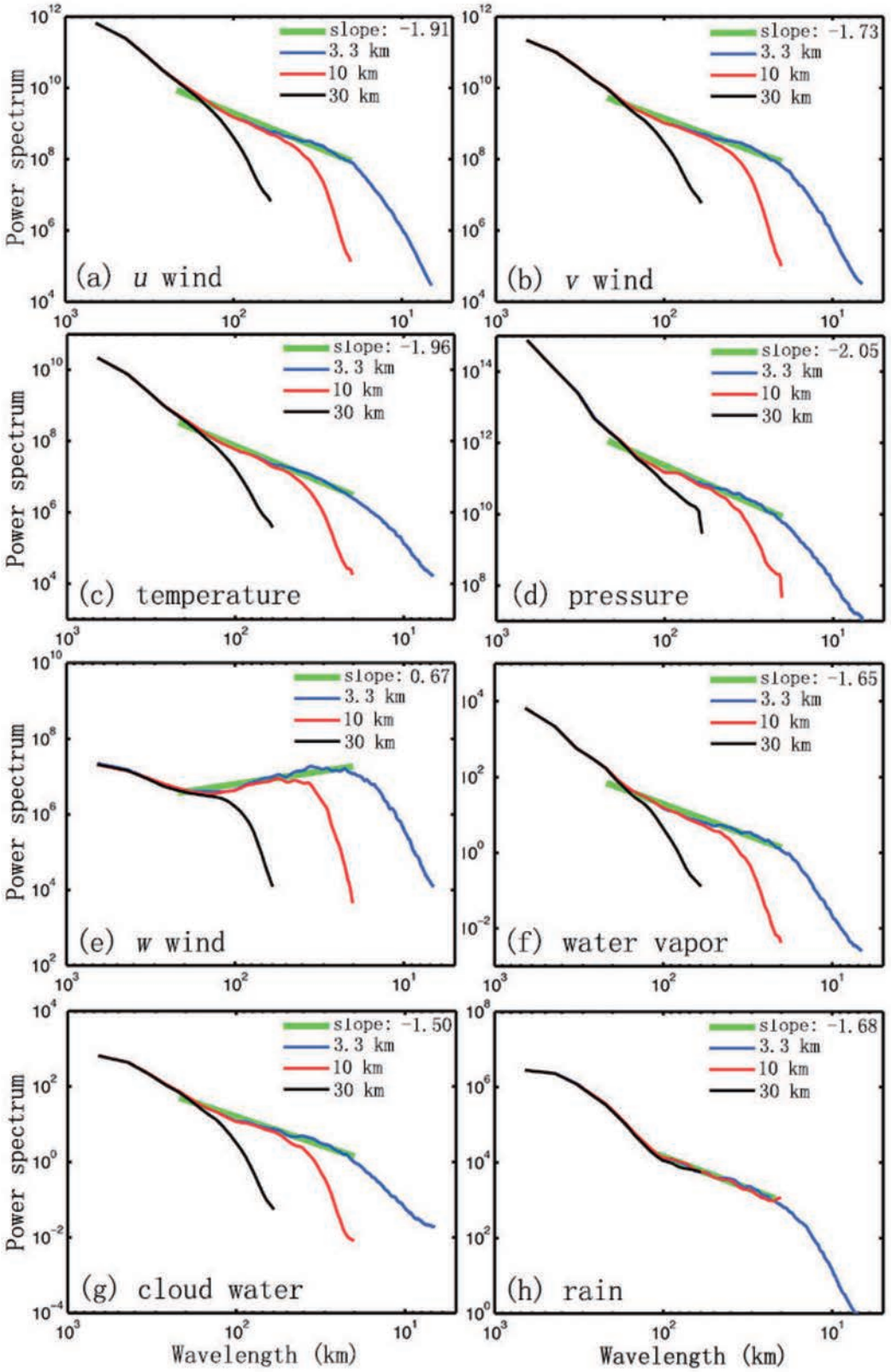

Fig. 3. The reference (total) spectra of different variables ($m^2\ s^{-2}$) with the model grid spacings of 30, 10 and 3.3 km, and the corresponding slope (green) between 20- and 200-km wavelengths.

energy will have to grow upscale. This is also one of the interpretations for the mesoscale spectrum, which is known as an inverse cascade of energy from the small-scale turbulence (Gage, 1979; Lilly, 1983; Vallis et al., 1997).

As defined in section 2, the loss of predictability index or LPI is defined as the ratio of the difference power spectra to

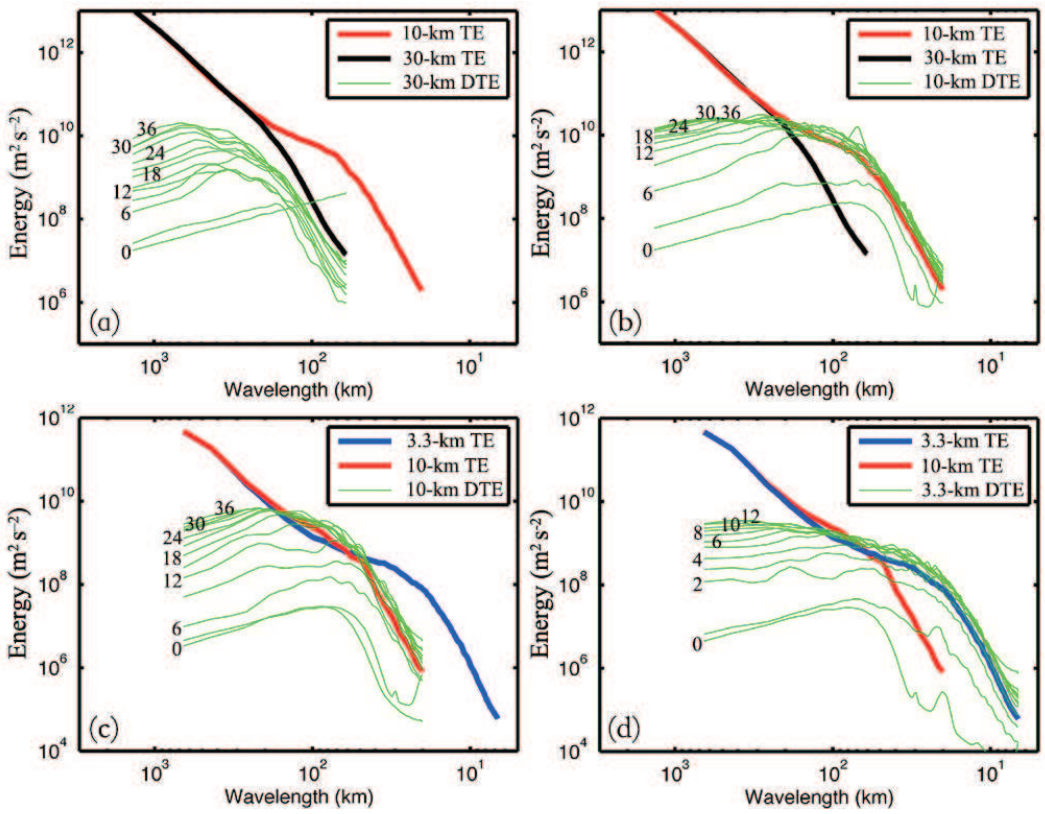

Fig. 4. (a, b) Spectra of difference total energy (green thin) and total energy (bold) with grid spacings of 30 and 10 km (red bold: 10 km; black bold: 30 km). (c, d) Spectra of difference total energy (green thin) and total energy (bold) with grid spacings of 10 and 3.3 km (red bold: 10 km; blue bold: 3.3 km) averaged over the same domain. The green lines (lower to upper) in (a–c) denote the difference spectra between lead times of 3 and 36 h at 3-h intervals. The green lines (lower to upper) in (d) denote the difference spectra between lead times of 1 and 12 h at 1-h intervals. The time sequence is denoted as digital numbers in the figures.

the reference-state power spectra. Thus, a larger (smaller) value of the LPI means less (more) predictability. Since the smallest resolvable scale of the model is seven times the model grid spacing, we select the scale of 220 km (just above the resolvable thresold for all three resolution runs) to compare the predictability of forecast variables at different model grid spacings. From the time evolution of the LPI of forecast variables at the model grid spacings of 3.3 km, 10 km and 30 km over the same domain and scale (∼220 km) (Fig. 5), the predictability of each variable varies with resolution. The difference of the maximum LPI value for forecast variables is remarkable around the scale of 220 km. In general, the difference in predictability estimates between the 10- and 3.3-km simulations (both considered convection-permitting with no parameterized convection) is smaller than those between the 30 and 10-km simulations (parameterized versus fully explict convection). Figure 5 also shows that the LPI of most of the variables with the grid spacing of 3.3 km is larger than those with the grid spacings of 10 km and 30 km during the first 3-h model integration, which is attributed to more rapid error growth and faster error saturation in high-resolution simulations (see Fig. 4). After 6 h, the LPI of all the variables with the grid spacing of 30 km is smaller than those with the grid spacings of 3.3 km and 10 km because there is little error growth from both parameterized and explicit convection in the 30-km simulation. In other words, the 30-km simulation with a smaller LPI at the earlier times results from the model's deficiency in resolving smaller scale (convective) instability at this resolution, and thus would lead to an overestimation of predictability. The 220-km scale is the marginal scale which can be resolved in a 30-km grid-spacing simulation, as evidenced in our reference power spectrum of Fig. 3, and consistent with the "effective resolution" study of Skamarock and Klemp (2008). Since the 30-km simulation does not explicitly permit moist convection or cannot directly resolve convective instability at smaller scales, it has a false sense of lower error growth at the small scales, resulting in an artificially lower LPI. Meanwhile, except for hydrometeors (cloud), the LPI of the other variables with the grid spacing of 3.3 km is smaller than those with the grid spacing of 10 km. This relates more deeply to the representation of moist convection by different resolutions since the convective instability is usually triggered at the smallest resolvable scale of the simulation (seven times the model grid spacing). The experiment with the 10-km grid spacing begins to permit direct simulation of the convective overturning [release of con-

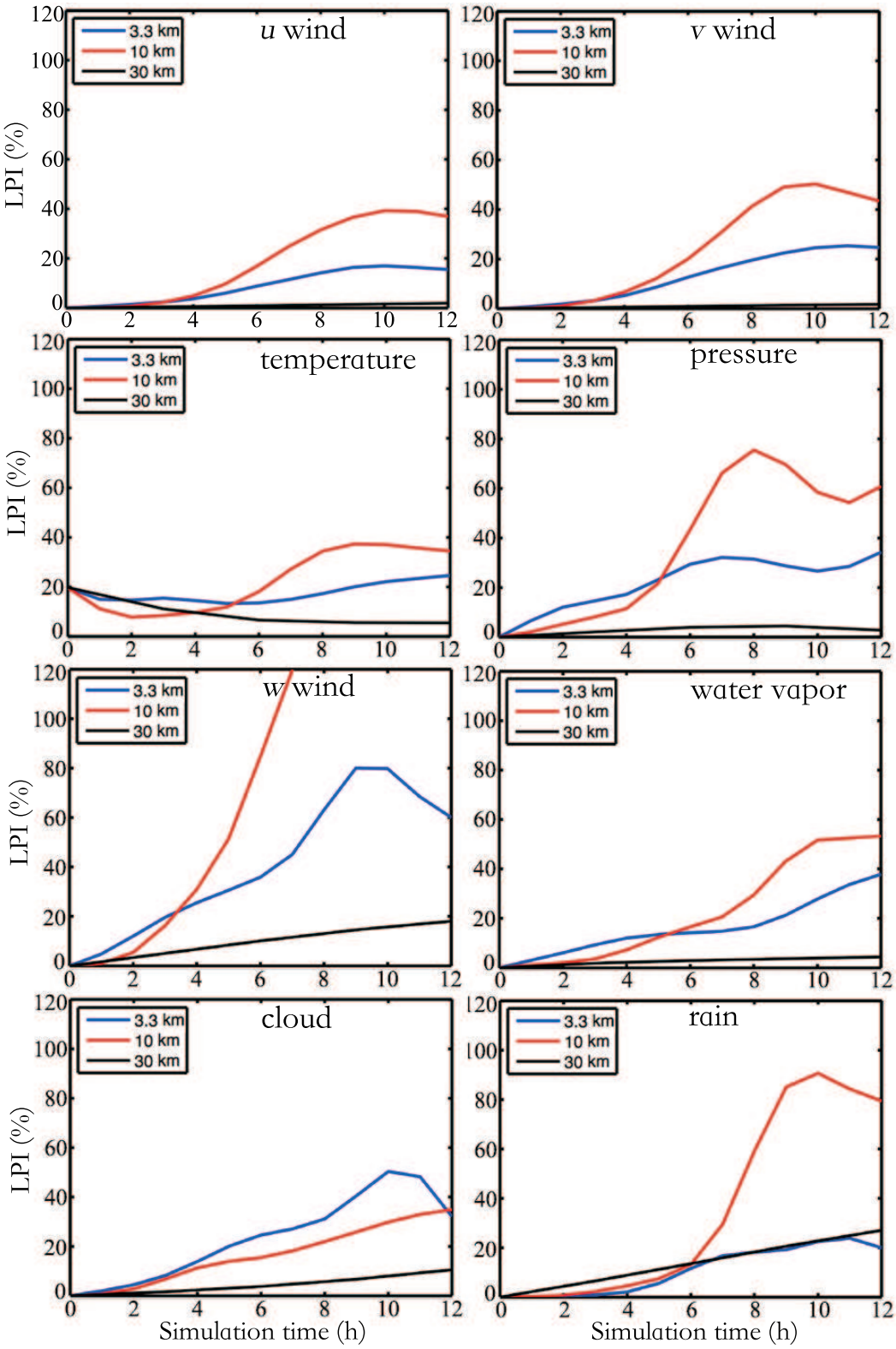

Fig. 5. Time evolution of LPI (%) for different forecast variables estimated from different grid spacings at the wavelength of 220 km.

vective available potential energy (CAPE)] at around 70 km, while the 3-km experiment maximizes the release of CAPE at around 23 km. In other words, during the moist convection, smaller scale error grows fastest at around 70 km in the experiment with the 10-km grid spacing, while error grows fastest at around 23 km in the experiment with the 3.3-km

grid spacing. Given the error for the 3.3-km grid spacing simulation saturates first at a smaller scale than for the 10-km grid-spacing simulation (23 km v.s. 70 km), it will take a longer time for the 3.3-km grid-spacing simulation to grow upscale and saturate at 70 km, and subsequently to impact the predictability at the 220-km scale. We believe this is the primary reason why the 3.3-km grid-spacing experiment has a lower LPI than the 10-km grid-spacing experiment, as shown in Fig. 5.

We also compare the time evolution of the LPI of forecast variables in the 10-km run and 30-km run at the same larger domain during a longer time period (figure not shown). The predictability difference between estimates with different resolutions for the variables related to large-scale processes (e.g., u, v, temperature, pressure, water vapor) is generally smaller than that for the variables associated with small-scale processes (e.g., w, cloud hydrometeors), which indicates that the predictability of the variables corresponding to small (large)-scale processes is more (less) sensitive to model resolution. Although all the variables (u, v, temperature, pressure, water vapor, w, cloud, and rain) are related to both large- and small-scale processes, the reference spectrum of each forecast variable reveals the strength of the spectral power of each variable at different scales. It is important to emphasize that the predictability of a given variable is related to its reference spectra distribution: the more energy at smaller scales, the less predictable that variable is, since smaller scale error grows faster and saturates early.

5. Scale- and variable-dependent error growth and predictability

In the previous section, we investigated the variability of the predictability index of forecast variables and the sensitivity of predictability to model resolutions. Here, we focus on the sensitivity of predictability to spatial scales (in terms of wavenumber or wavelength) for each forecast variable, exclusively using the pair of 10-km simulations. By definition, when the LPI is equal to or greater than 100%, there is a complete loss of predictability, while a forecast with a smaller LPI of less than 100% at least has some degree of predictability.

Figure 6 presents the LPI of forecast variables at four different scales, indicating that the predictability of forecast variables is associated closely with their corresponding background (reference-state) spectra (see Fig. 3), varying significantly with variables. As exemplified in the 200-km and 300-km LPI (Figs. 6b and c), in general, the variables with more small-scale components (such as vertical velocity and hydrometeors, shown in Figs. 3e and g, respectively) are less

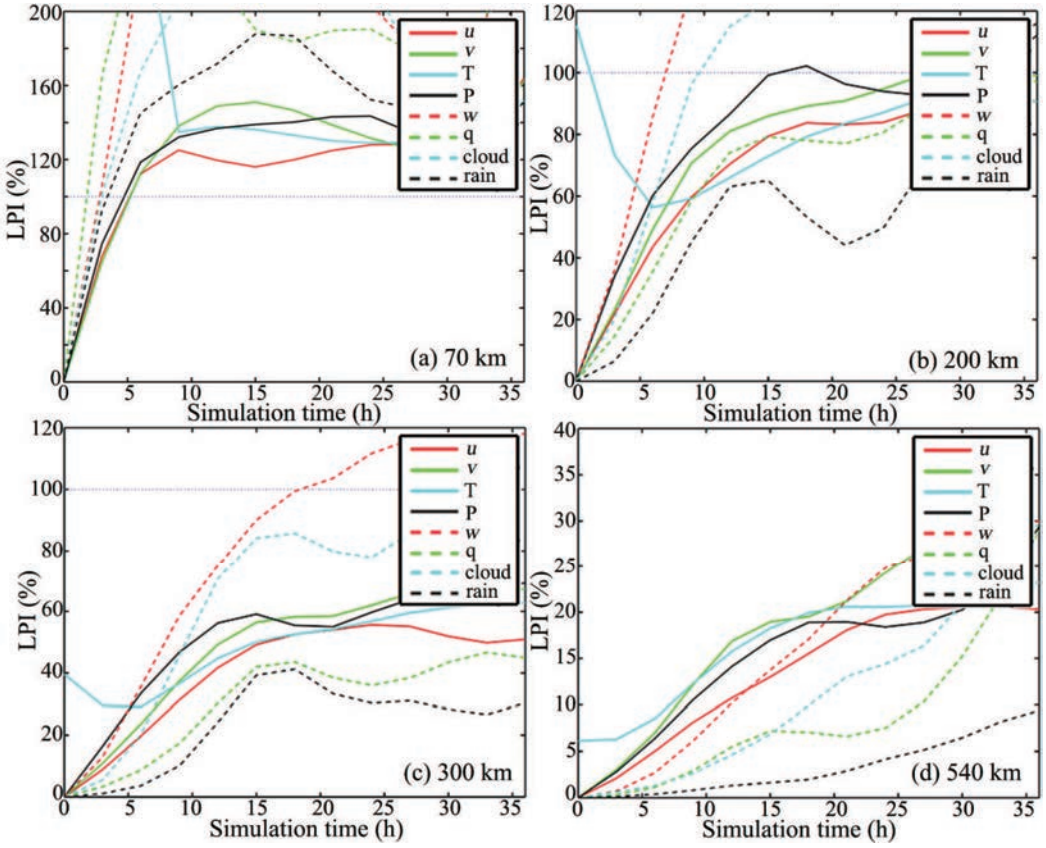

Fig. 6. Time evolution of the LPI for the variables u (red solid), v (green solid), temperature (blue solid), pressure (black solid), w (red dashed), q (green dashed), cloud (blue dashed), and rain (black dashed) at the scales of (a) 70 km, (b) 200 km, (c) 300 km, and (d) 540 km from the 10-km domain.

predictable, and vice versa [e.g., u,v, temperature (T), and pressure (P), shown in Figs. 3a–d, respectively]. For a particular variable, the LPI usually increases with forecast lead time at a selected scale: the longer the lead time, the less predictable the variable, which is consistent with Islam et al. (1993, Fig. 5). The only exception is a high LPI value of variable temperature (T) during the first 6 h, because the only initial perturbations between perturbed and reference simulations are added to T, which will be initially adjusted. In addition, the high LPI of T during the first 6 h decreases as the scale increases since "grid-point (grid by grid data set)", random, Gaussian noises with zero mean and a standard deviation of 0.2 K are added to the temperature field at the initial time in the perturbed runs. At the scale of 70 km (Fig. 6a), the LPI of all variables reaches 100% after only a 5-h forecast lead time. At the scale of 200 km (Fig. 6b), the LPI values of all the variables become lower in comparison with those at the scale of 70 km, which means higher predictability. The variability of the predictability among forecast variables is also larger. The LPI of vertical velocity and hydrometeors are much larger than those of other variables, with the predictable times of 7 and 9 h at this scale, respectively. At the scale of 300 km (Fig. 6c), variables u,v, temperature, pressure, q and rain (3-h precipitation) have a predictable time of more than 36 h—roughly 72 h as estimated through the current trend in Fig. 6c. The predictable time for vertical velocity is about 15 h. At the scale of 540 km (Fig. 6d), all the variables, including vertical velocity, have a predictable time of more than 36 h.

The LPI time evolutions at different scales for the 3.3-km run are shown in Fig. 7. In general, it is consistent with the result from the 10-km run. For example, the LPI values of variables w and cloud are usually higher (and thus less predictable) than those of other variables at the scales for 200 km and 300 km. It is interesting to note that the LPI values of all forecast variables in the 3.3-km run are lower (implying a potentially more predictable estimate) than those estimated by the 10-km run, despite the fact that the error grows faster in the 3.3-km run (since LPI measures the related rate of error growth normalized by the reference state spectral power). According to the definition of LPI (the ratio of the difference or forecast error spectral power to the reference spectral power at a given scale or a range of scales), the value of LPI is decided by both the difference and reference spectral power at a given scale or range of scales. In section 4, we found the error grows faster at smaller scales in higher-resolution simulations, but the reference spectral power at smaller scales is also larger than that of lower-resolution simulations for a given scale as shown in Fig. 4. Therefore, the LPI value for a given scale can still be lower (indicating higher predictabil-

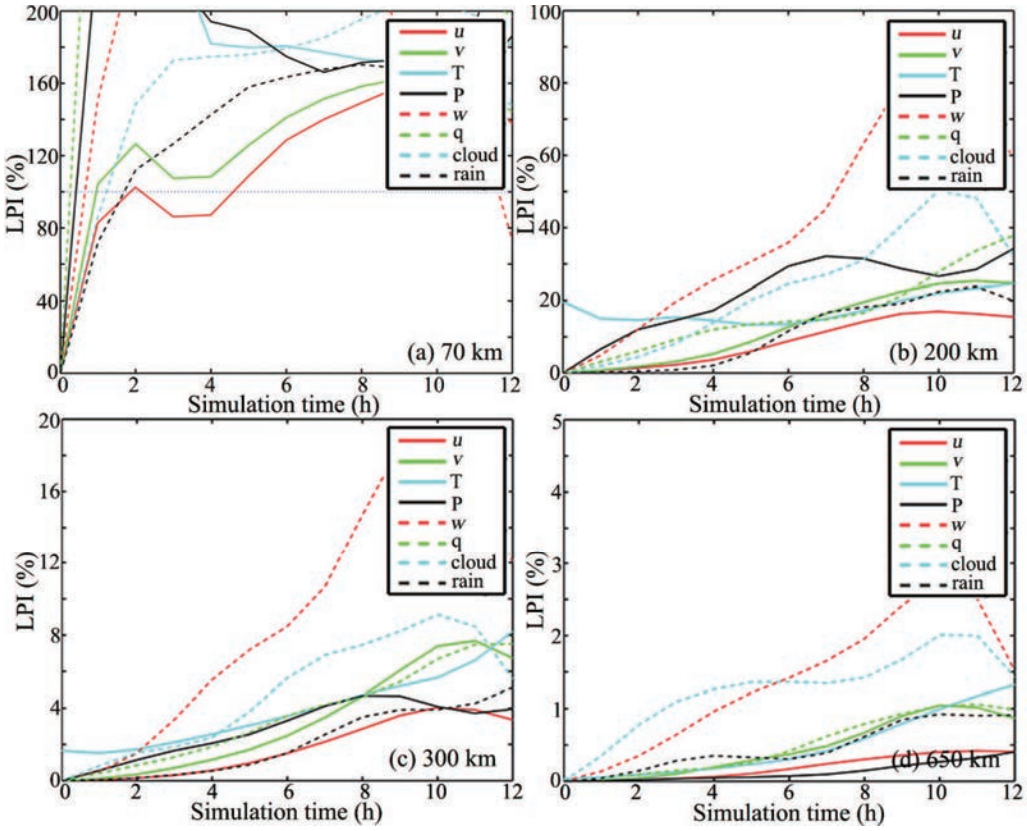

Fig. 7. Time evolution of the LPI for the variables u (red solid), v (green solid), temperature (blue solid), pressure (black solid), w (red dashed), q (green dashed), cloud (blue dashed), and rain (black dashed) at the scales of (a) 70 km, (b) 200 km, (c) 300 km, and (d) 650 km from the 3.3-km domain.

ity) than that of lower-resolution simulations, as shown in Figs. 6 and 7.

6. Further interpretations of LPI in physical space

In this section we provide further interpretations of the LPI values in physical space (versus the wavenumber space or spectral power described in previous sections). We use the same 2D spectral decomposition (as introduced in section 2) to divide the difference (between perturbed and unperturbed runs) and total fields (unperturbed run) into five horizontal scale bands (in the physical space through inverse 2D Fourier transform, which include scales smaller than 200 km, from 200 to 500 km, from 500 to 1000 km, from 1000 to 2000 km, and larger than 2000 km. We concentrate on meridional wind (v), which has more larger-scale spectral power, and vertical velocity (w), which has more smaller-scale spectral power. The 2D spectral decomposition in this section is conducted with the model output from the D3 domain with the grid spacing of 10 km.

Figure 8a shows the time evolution of the domain-integrated DTE at these five scale bands. Before 9 h, the DTE at scales smaller than 200 km contributes the most to the total DTE; while after 9 h, the DTE at scales from 200 and 500 km contribute the most to the total DTE. DTE at scales smaller than 500 km account for more than 75% of the total DTE during the whole simulation period. For the time evolution of total energy (Fig. 8b), its magnitude increases with scale. In addition, the difference power spectra at different scales vary among variables. For example, the time evolution of the difference power spectra of u, v, T and P are quite similar (not shown). For vertical velocity (w) and hydrometeors (cloud), difference power spectra at scales below 500 km account for more than 90% of the total difference power spectra. The vertical distribution of difference power spectra also varies remarkably among variables, indicating the variation of the LPI (and thus difference in predictability) for different variables at different altitudes. Since the trend of DTE is similar at scales from 200 to 500 km and from 500 to 1000 km, we focus only on these three horizontal scale bands, including scales smaller than 200 km, from 200 to 1000 km and larger than 1000 km. The vertical distributions of the domain-averaged LPI of variables v and w at these scales are shown in Fig. 9. The LPI varies with height and lead time for different variables. For scales larger than 1000 km, the LPI of variable v over all layers and the LPI of variable w at layers under a height of 5 km is very small. However, the LPI increases with decreasing scale. The LPI at upper layers is generally much higher than that at lower layers.

In terms of the distribution of the physical field, the difference field can have similar (or larger) amplitude (spatial coverage) with (than) the reference field when the LPI is equals to or is larger than 100%, which means over-prediction of magnitude or missing predictions of location in practical prediction evaluation. For scales smaller than 200 km, the

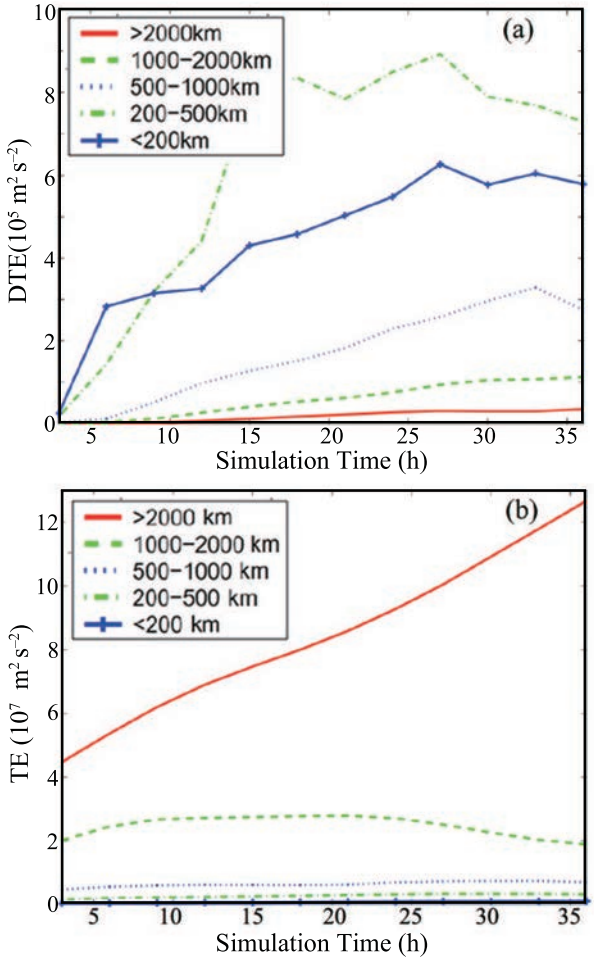

Fig. 8. Time evolution of (a) DTE (m^2 s^{-2}) and (b) TE (total energy: m^2 s^{-2}) at different scales.

difference field vs. the reference field of v (at a height of 3.5-km), w (at a height of 5 km) at 3 h and 6 h are shown in Fig. 10. At 3 h (Figs. 10a–d), the magnitude of the difference v (w) component is comparable to the reference v (w) component, while the spatial coverage is smaller. The related domain-wide averaged LPI of v (w) is 10% (50%) at 3 h. At 6 h (Figs. 10e–h), both the magnitude and distribution are very similar between the difference and total fields. The related domain-wide averaged LPI of v (w) is 120% (170%) at 6 h, showing that variables v and w are completely unpredictable at this scale (< 200 km) at the lead time of 6 h. There is a similar evolution in other variables at this scale. For the scale from 200 to 1000 km, the magnitude and spatial coverage of difference fields are both smaller than those of the reference field at a height of 3.5 km (v) and 5 km (w) (not shown). For variable v, the domain-averaged predictability indices are 5% at 6 h and 15% at 24 h. For variable w, the related domain-averaged predictability indices are 20% at 6 h and 60% at 24 h. At the scale larger than 1000 km (not shown), for variable v, the magnitude and spatial coverage of the difference field are both smaller than those of the reference field. For variable w, the difference field has an obvious increase above a

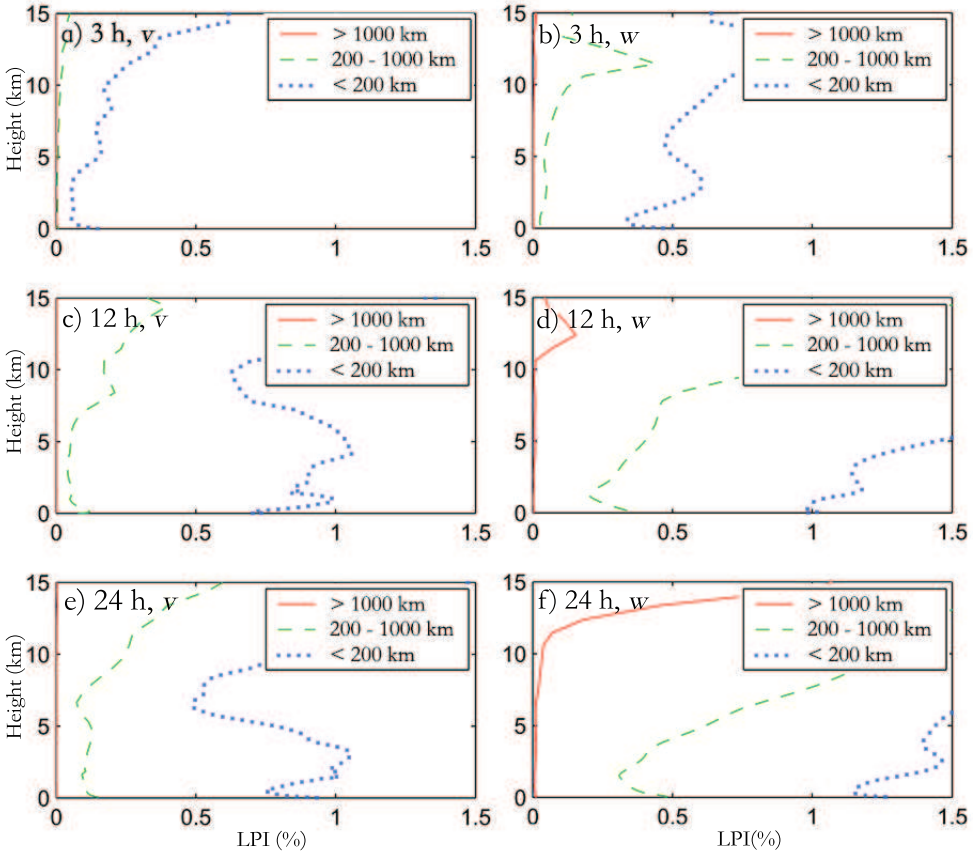

Fig. 9. Vertical profile of the predictability index (LPI) averaged over the entire domain for variables *v* (a, c, e) and *w* (b, d, f) at three scales (blue: $<$ 200 km; green: 200–1000 km; red: $>$ 1000 km).

height of 10 km. These results indicate that the value of the LPI is dependent on the magnitude and spatial coverage of difference variables.

7. Conclusions

In this study, we quantified and compared the predictability of different forecast variables at various scales through spectral analysis by using perturbed and unperturbed simulation outputs of the idealized moist baroclinic waves amplifying in a conditionally unstable atmosphere with varying model grid spacing. An index named LPI was defined to quantify the predictability of forecast variables based on the reference spectrum of forecast variables. Further interpretations of the LPI in physical space were provided through a two-dimensional spectral decomposition.

We first analyzed the slope of the spectrum represented by different forecast variables and found that predictability of forecast variables is closely associated with their corresponding reference-state (unperturbed) power spectrum and slope, which differ significantly from variable to variable. The shallower the reference-state spectrum, the more spectral energy resides at smaller scales, and thus the lower the predictability for any given variable, since the error grows faster at smaller scales before it saturates. In general, the variables with more small-scale components (e.g., vertical velocity) are less predictable, and vice versa (e.g., pressure). For a specific variable, the LPI generally increases with forecast lead time at the same scale, and the longer the lead time, the less predictable the variable, which is consistent with Islam et al. (1993), except for the high LPI value of variable *T* during the adjustment time in this study.

We further analyzed the spectral distribution of the forecast variables in the reference simulation at different model resolutions, showing that the spectrum of the reference state differs significantly among forecast variables and with model resolutions. The LPI values of all forecast variables estimated by the grid spacing of 3.3 km are lower (indicating higher predictability) than those estimated by the grid spacing of 10 km, despite the fact that the error grows faster in the 3.3-km run. In terms of difference total energy, the error grows faster in the higher-resolution simulations and spreads to larger scales more quickly before the error saturates at those small scales during the first few hours of the simulations. The maximum values of LPI of forecast variables deviate notably from each other and change with model resolution.

Lastly, we explained the meaning of the LPI in physical space through a 2D spectral decomposition. For the first time, we showed the difference field vs the reference field of the variables *v* and *w* at the time with different LPI values.

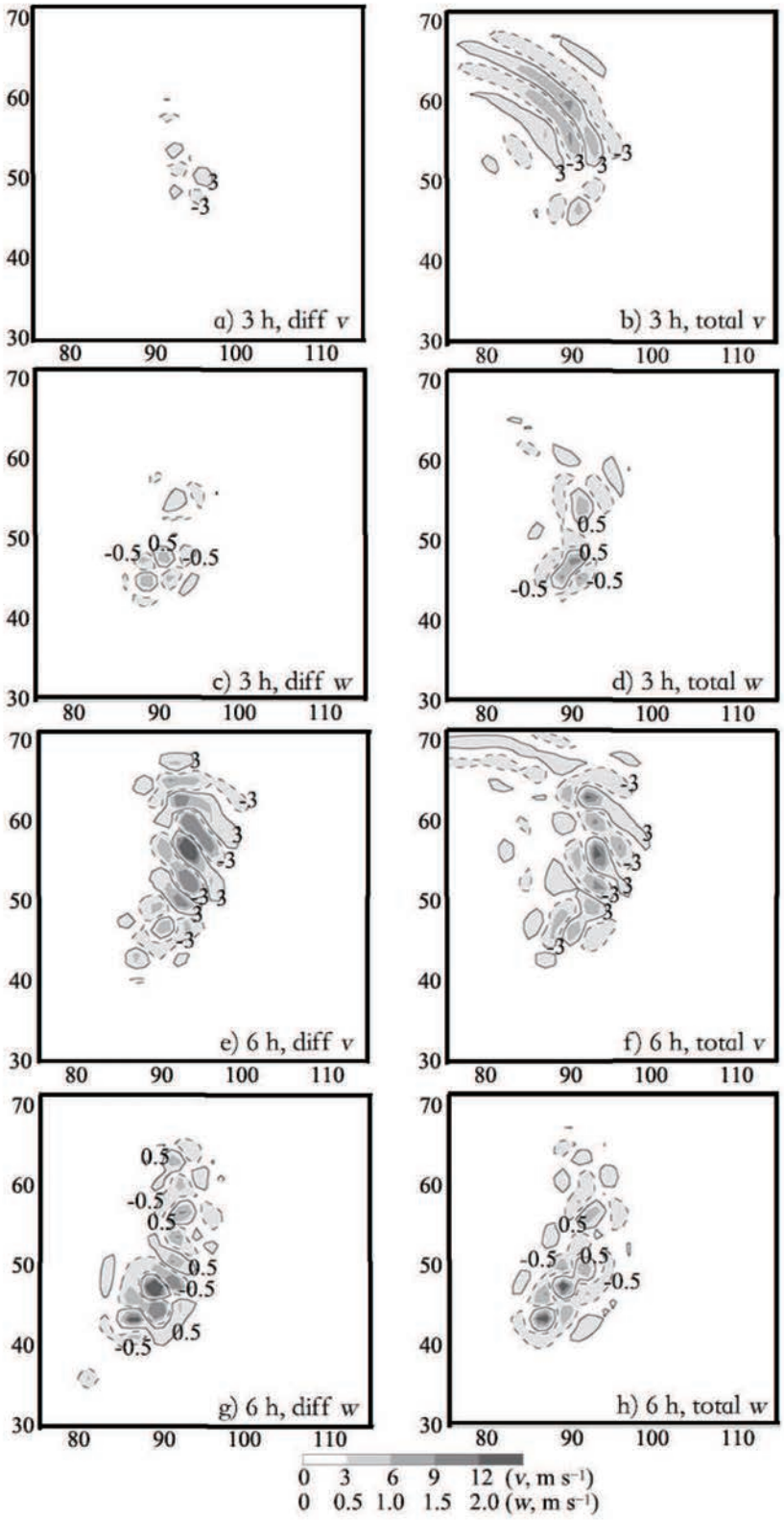

Fig. 10. The difference (a, c, e, g) and reference (b, d, f, h) fields of variable *v* (at 3.5 km) and *w* (at 5 km) at scales below 200 km at 3 h and 6 h. The *x*–*y* coordinates denote the number of model grids in domain D3.The contours (solid: positive; dashed: negative) are every 3 m s^{-1} (0.5 m s^{-1}) for the difference and reference field of variable *v* (*w*). The shading key in panel (a) denotes the magnitude of difference and reference fields of variables *v* and *w*, respectively. The digit numbers on x-axis and y-axis 90 km.

Physically, the value of the LPI is dependent on the magnitude and spatial coverage of difference fields. An LPI value at or above 100% denotes over-prediction of magnitude or a missing prediction in practical prediction evaluations.

The current study on variable- and scale-dependent predictability was based only on simulations of one idealized moist baroclinic wave life cycle. Further research based on measurement case studies through ensemble experiments will be very helpful for improving quantitative forecasts in operational forecasting. The LPI defined in this study can be used in future operational forecasting.

Acknowledgements. This research was funded by the National Natural Science Foundation of China (Grant No. 41275101) and the Fundamental Research Funds for the Central Universities of China. It was also supported by the US NSF (Grant Nos. ATM-0618662 and ATM-0904635) and the US Office of Naval Research (Grant No. N00014-09-1-0526).

REFERENCES

Anthes, R. A., Y. H. Kuo, D. P. Baumhefner, R. P. Errico, and T. W. Bettge, 1985: Predictability of mesoscale atmospheric motions. *Advances in Geophysics*, **28B**, 159–202.

Bartello, P., 2010: Quasigeostrophic and stratified turbulence in the atmosphere. IUTAN Symposium on Turbulence in the Atmosphere and Oceans, D. G. Dritschel, Ed., Springer, Vol. IUTAM Bookseries 28, 117–130.

Bei, N. F., and F. Q. Zhang, 2007: Impacts of initial condition errors on mesoscale predictability of heavy precipitation along the Mei-Yu front of China. *Quart. J. Roy. Meteor. Soc.*, **133**, 83–99.

Charney, J. G., 1971: Geostrophic turbulence. *J. Atmos. Sci.*, **28**, 1087–1095.

Charney, J. G., R. G. Fleagle, H. Riehl, V. E. Lally, and D. Q. Wark, 1966: The feasibility of a global observation and analysis experiment. *Bull. Amer. Meteor. Soc.*, **47**, 200–220.

Cho, J. Y. N., and Coauthors, 1999: Horizontal wavenumber spectra of winds, temperature, and trace gases during the Pacific Exploratory Missions: 1. Climatology. *J. Geophys. Res.*, **104**, 5697–5716.

Dewan, E. M., 1979: Stratospheric spectra resembling turbulence. *Science*, **402**, 832–835.

Ehrendorfer, M., R. M. Errico, and K. D. Raeder, 1999: Singular-vector perturbation growth in a primitive equation model with moist physics. *J. Atmos. Sci.*, **56**, 1627–1648.

Errico, R. M., and D. P. Baumhefner, 1987: Predictability experiments using a high-resolution limited area model. *Mon. Wea. Rev.*, **115**, 488–504.

Dudhia, J., 1993: A nonhydrostatic version of the Penn State-NCAR Mesoscale Model: Validation tests and simulation of an Atlantic cyclone and cold front. *Mon. Wea. Rev.*, **121**, 1493–1513.

Gage, K. S., 1979: Evidence for a $k^{-5/3}$ law inertial range in mesoscale two-dimensional turbulence. *J. Atmos. Sci.*, **36**, 1950–1954.

Grell, G. A., 1993: Prognostic evaluation of assumptions used by cumulus parameterizations. *Mon. Wea. Rev.*, **121**, 764–787.

Hamilton, K., Y. O. Takahashi, and W. Ohfuchi, 2008: The mesoscale spectrum of atmospheric motions investigated in a very fine resolution global general circulation model. *J. Geophys. Res.*, **113** (D18), doi: 10.1029/2008JD009785.

Hohenegger, C., and C. Schär, 2007: Predictability and error growth dynamics in cloud-resolving models. *J. Atmos. Sci.*, **64**, 4467–4478.

Hong, S.-Y., and H. L. Pan, 1996: Nonlocal boundary layer vertical diffusion in a medium-range forecast model. *Mon. Wea. Rev.*, **124**, 2322–2339.

Islam, S., R. L. Bras, and K. A. Emanuel, 1993: Predictability of mesoscale rainfall in the tropics. *J. Appl. Meteor.*, **32**, 297–310.

Kitamura, Y. and Y. Matsuda, 2010: Energy cascade processes in rotating stratified turbulence with application to the atmospheric mesoscale. *J. Geophys. Res.*, **115**, D11104, doi: 10.1029/2009JD012368.

Koshyk, J. N., and K. Hamilton, 2001: The horizontal kinetic energy spectrum and spectral budget simulated by a high-resolution troposphere-stratosphere-mesosphere GCM. *J. Atmos. Sci.*, **58**, 329–348.

Leith, C. E., 1965: *Numerical Simulation of the Earth's Atmosphere*. Vol. 4, *Methods in Computational Physics*, Academic Press, 1–28.

Lilly, D. K., 1983: Stratified turbulence and the mesoscale variability of the atmosphere. *J. Atmos. Sci.*, **40**, 749–761.

Lindborg, E., 2006: The energy cascade in a strongly stratified fluid. *J. Fluid Mech.*, **550**, 207–242.

Lindborg, E., 2007: Horizontal wavenumber spectra of vertical vorticity and horizontal divergence in the upper troposphere and lower stratosphere. *J. Atmos. Sci.*, **64**, 1017–1025.

Lindborg, E., and J. Y. N. Cho, 2001: Horizontal velocity structure functions in the upper troposphere and lower stratosphere: 2. Theoretical considerations, *J. Geophys. Res.*, **106**, 10 233–10 241.

Lorenz, E. N., 1969: The predictability of a flow which possesses many scales of motion. *Tellus*, **21**, 289–307.

Lorenz, E. N., 1982: Atmospheric predictability experiments with a large numerical model. *Tellus*, **34**, 505–513.

Morss, R. E., C. Snyder, and R. Rotunno, 2009: Spectra, spatial scales, and predictability in a quasigeostrophic model. *J. Atmos. Sci.*, **66**, 3115–3130.

Nastrom, G. D. and K. S. Gage, 1985: A climatology of atmospheric wavenumber spectra observed by commercial aircraft. *J. Atmos. Sci.*, **42**, 950–960.

Rotunno, R., and J. W. Bao, 1996: A case study of cyclogenesis using a model hierarch. *Mon. Wea. Rev.*, **124**, 1051–1066.

Rotunno, R., and C. Snyder, 2008: A generalization of Lorenz's model for the predictability of flows with many scales of motion. *J. Atmos. Sci.*, **65**, 1063–1076.

Shukla, J., 1981: Dynamical predictability of monthly means. *J. Atmos. Sci.*, **38**, 2547–2572.

Skamarock, W. C., 2004: Evaluating mesoscale NWP models using kinetic energy spectra. *Mon. Wea. Rev.*, **132**, 3019–3032.

Skamarock, W. C., and J. B. Klemp, 2008: A time-split nonhydrostatic atmospheric model for weather research and forecasting applications. *J. Comput. Phys.*, **227**, 3465–3485.

Smagorinsky, J., 1969: Problems and promises of deterministic extended-range forecasting. *Bull. Amer. Meteor. Soc.*, **50**, 286–311.

Tan, Z. M., F. Q. Zhang, R. Rotunno, and C. Snyder, 2004: Mesoscale predictability of moist baroclinic waves: Experiments with parameterized convection. *J. Atmos. Sci.*, **61**, 1794–1804.

Tennekes, H., 1978: Turbulent flow in two and three dimensions. *Bull. Amer. Meteor. Soc.*, **59**, 22–28.

Tulloch, R., and K. S. Smith, 2006: A theory for the atmospheric energy spectrum: Depth-limited temperature anomalies at the tropopause. *Proc. Natl. Acad. Sci. USA*, **103**, 14 690–14 694.

Tulloch, R., and K. S. Smith, 2009: Quasigeostrophic turbulence with explicit surface dynamics: Application to the atmospheric energy spectrum. *J. Atmos. Sci.*, **66**, 450–467.

Tung, K. K. and W. W. Orlando, 2003: The k^{-3} and $k^{-5/3}$ energy spectrum of atmospheric turbulence: Quasigeostrophic two-level model simulation. *J. Atmos. Sci.*, **60**, 824–835.

Vallis, G. K., G. J. Schutts, and M. E. B. Gray, 1997: Balanced mesoscale motion and stratified turbulence forced by convection. *Quart. J. Roy. Meteor. Soc.*, **123**, 1621–1652.

VanZandt, T. E., 1982: A universal spectrum of buoyancy waves in the atmosphere. *Geophys. Res. Lett.*, **9**, 575–578.

Vukicevic, T., and R. M. Errico, 1990: The influence of artificial and physical factors upon predictability estimates using a complex limited-area model. *Mon. Wea. Rev.*, **118**, 1460–1482.

Waite, M., and C. Snyder, 2013: Mesoscale energy spectra of moist baroclinic waves. *J. Atmos. Sci.*, **70**, 1242–1256.

Warner, T. T., D. Keyser, and L. W. Uccellini, 1983: Some practical insights into the relationship between initial state uncertainty and mesoscale predictability. *Proc. Conf. Predictability of Fluid Motions*, La Jolla, California, American Institute of Physics, 271–286.

Yuan, L., and K. P. Hamilton, 1994: Equilibrium dynamics in a forced-dissipative f-plane shallow-water system. *J. Fluid. Mech.*, **280**, 369–394.

Zhang, F., C. Snyder, and R. Rotunno, 2002: Mesoscale predictability of the "surprise" 24–25 January 2000 snowstorm. *Mon. Wea. Rev.*, **130**, 1617–1632.

Zhang, F., and C. Snyder, 2003: Effects of moist convection on mesoscale predictability. *J. Atmos. Sci.*, **60**, 1173–1185.

Zhang, F., C. Snyder, A. M. Odins, and J. W. Nielsen-Gammon, 2006: Mesoscale predictability of an extreme warm-season precipitation event. *Wea. Forecasting*, **21**, 149–166.

Zhang, F., N. Bei, R. Rotunno, C. Snyder, and C. C. Epifanio, 2007: Mesoscale predictability of Moist Baroclinic Waves: Convection-permitting experiments and multistage error growth dynamics. *J. Atmos. Sci.*, **64**, 3579–3594.